The effects of field history on magnetic skyrmion formation in $[Pt/Co/Ir]_3$ multilayers

Andy T. Clark[1], X. Wang[1], A. R. Stuart[2], Q. Wang[3], W. Jiang[4,5], J. E. Pearson[4], S. G. E. te Velthuis[4], A. Hoffmann[4,6], X. M. Cheng[1*], K. S. Buchanan[2,*]

1. Department of Physics, Bryn Mawr College, Bryn Mawr, PA, USA
2. Department of Physics, Colorado State University, Fort Collins, CO, USA
3. Department of Physics and Astronomy, West Virginia University, Morgantown, WV, USA
4. Materials Science Division, Argonne National Laboratory, Lemont, IL, USA
5. Department of Physics, Tsinghua University, Beijing, China
6. Department of Materials Science and Engineering, University of Illinois at Urbana-Champaign, Urbana, IL, USA

Abstract

We report on the formation of Néel-type magnetic bubble skyrmions at room temperature in $[Pt/Co/Ir]_3$ multilayered thin films after an in-plane magnetic field treatment. Polar magneto-optical Kerr Effect (p-MOKE) microscopy images show that the dendritic magnetic configurations observed after AC demagnetization evolve into magnetic bubble skyrmions after the application and subsequent removal of an in-plane magnetic field. Micromagnetic simulations were used to systematically investigate the role of the in-plane magnetic field magnitude, misalignment of the sample, and the Dzyaloshinskii-Moriya interactions (DMI) in generating bubble skyrmions during the field treatment. The simulations show that in-plane fields slightly below the saturation field are the most effective at producing skyrmions, and, furthermore, a small field angle away from the sample plane not only leads to improved skyrmion formation but also provides a means to select the skyrmion polarity where the direction of the out-of-plane component of the field is opposite to the direction of the skyrmion cores. This field treatment scheme leads to a simple and reliable way to create magnetic bubble skyrmions in multilayered thin films with DMI.

Keywords: magnetic skyrmions, micromagnetic simulations, antisymmetric exchange

Introduction

Magnetic skyrmions have attracted great interest due to their potential for storage, logic, and neuromorphic computing applications [1,2], and for exploring fundamental physics involving the Dzyaloshinskii-Moriya interactions (DMI)[3,4]. Magnetic skyrmions [5], first observed in B20 materials with bulk DMI[6,7], are also known to readily form in ferromagnetic/heavy metal (FM/HM) layered thin films with interfacial DMI[8–11]. Multilayered thin films with interfacial DMIs have enabled the formation of stable skyrmions at room temperature, for example in $[Pt/Co/HM]_n$ multilayers, where the HM layer is W, Ir, or Ta[12–15]. The skyrmions observed in multilayered films are usually bubble skyrmions that are made up of small, circular or quasi-circular cores surrounded by chiral domain walls that are typically Néel-type, though the wall type may vary with depth in a multilayer with a large repeat number n [16].

In order to study skyrmions and to develop applications, reliable methods for skyrmion creation must be developed and the formation mechanisms must be understood. Methods for creating skyrmions on demand via spin transfer torque due to local current injection[17,18] and via the spin Hall effect at a narrow constriction have been described[9,19]. Lithographic patterning of magnetically soft cylindrical disks on top of a film with perpendicular anisotropy has also been used as a strategy to create skyrmions at controlled locations and can be employed even in the absence of DMI [11]. Skyrmions have also been generated and controlled using voltage-controlled magnetic anisotropy[20], and field-free writing/deleting of skyrmions by hydrogen chemisorption/desorption that modifies the anisotropy of the magnetic material has been demonstrated[21]. Magnetic fields can also be used to promote skyrmion formation more globally. Experiments on a W/CoFeB/Ta/MgO wedge sample have shown that narrow but not wide stripe domains can be transformed into bubble states after the application of an out-of-plane field, and that an in-plane magnetic field will cause stripe domains to narrow consequently improves the likelihood of skyrmion formation through a stripe-breaking mechanism that is facilitated by the DMI[22]. A bubble domain phase has also been observed after specific field treatment protocols for a narrow thickness range in ultrathin wedged Fe/Ni bilayer films grown on Cu(001) substrates that have perpendicular anisotropy[23] but likely weaker DMI since there is no source of strong spin orbit coupling in the bilayer[24].

Here, we investigate the formation of magnetic skyrmions in sputter-deposited multilayered films of $[Pt/Co/Ir]_3$ using a simple field treatment scheme that involves a demagnetization step followed by the application and removal of an in-plane field that is slightly below the magnetic saturation field, and we explain how the formation process works. Micromagnetic simulations provide insight into the role of the DMI in the skyrmion formation process as well as the importance of the field magnitude and angle. This work provides guidance for how to improve skyrmion formation using a simple strategy that only involves a magnetic field, and this field-treatment method is suitable for preparing a large number of skyrmions in multilayer thin films with interfacial DMI.

Methods

Skyrmion formation was investigated experimentally in a substrate/Ta(2nm)/[Pt (1.5nm)/Co (1nm)/Ir (1nm)]$_3$/Pt (2 nm) thin film multilayer, illustrated in Fig. 1(a) and referred to as $[Pt/Co/Ir]_3$. The multilayer sample was deposited onto a Si substrate with a 300-nm-thick thermally oxidized SiO_2 top layer by DC magnetron sputtering using deposition rates for Ta, Pt, Co and Ir of 0.4, 0.5, 0.2, and 0.4 Å/s, respectively. The base pressure was about 5×10^{-8} Torr, and the deposition pressure was 5 mTorr with an Ar gas flow rate of 30 SCCM. X-ray reflectivity (XRR) measurements were performed using a Rigaku Ultima IV x-ray diffractometer to confirm the periodicity of the multilayer films, and hysteresis loops were measured with the field out-of-plane (easy axis) using a vibrating sample magnetometer, and in-plane using a superconducting quantum interference device (SQUID) magnetometer to obtain the saturation magnetization and magnetic anisotropy of the sample. The SQUID magnetometer was used for the latter because a higher in-plane magnetic field was needed to saturate the sample.

To set the samples into a demagnetized state, AC demagnetization was performed with a damped oscillating magnetic field applied normal to the sample plane. Polar magneto-optical Kerr effect (p-MOKE) microscopy with an evicomagnetics MOKE microscope was used to image the $[Pt/Co/Ir]_3$ multilayer at room temperature and zero magnetic field first after the AC demagnetization, and subsequently after a field treatment procedure that involved applying an in-plane magnetic field of $\mu_o H_{max}$ = 0.9 T and then turning it off. The uncertainty in the sample alignment during the in-plane field treatment was $\sim \pm 3°$.

Micromagnetic simulations were conducted using MuMax^3 [25] to gain insight into the skyrmion formation process. The simulations were done using saturation magnetization and uniaxial anisotropy values of $M_s = 1.1 \times 10^6$ A/m and $K_u = 1.4 \times 10^6$ J/m^3 with an out-of-plane easy axis, respectively. These values were extracted from magnetometry measurements of the $[Pt/Co/Ir]_3$ films (Fig. 1(c)). The $[Pt/Co/Ir]_3$ multilayers were modeled as a single 3-nm thick film with lateral dimensions of 2048 nm, and periodic boundary conditions were used to extend the lateral dimensions of the film by a factor of four. A cell size of $(2 \times 2 \times 3)$ nm^3 was used. The simulations were repeated with three separate 1-nm thick Co layers with weak ferromagnetic interlayer coupling and the results were qualitatively similar, but the single layer simulations are faster. The exchange stiffness A_{ex} was set to 10 pJ/m, and DMI values of $D = 1.6$ mJ/m^2 [13], 2.1 mJ/m^2[26], and 0 mJ/m^2 were used to determine the effects of DMI on the skyrmion formation.

The simulations were conducted by first relaxing the magnetic film from a random magnetization state in zero magnetic field by using the MuMax relax function[25]. Next, an out-of-plane damped AC magnetic field was applied using a damped cosine function $A\cos(2\pi f t)\, e^{(-t/\tau)}$ with amplitude A = 0.1 T, frequency f = 0.33 GHz, and damping time τ = 5 ns. The simulations were time-evolved using the run command for 30 ns with a damping constant of $\alpha = 0$ and the resulting AC demagnetized states at 30 ns (e.g., Fig. 2(d)) were used as the input state for the subsequent in-plane field treatments. This sequence of a random initial condition followed by an AC demagnetization sequence was chosen to replicate the experimental AC demagnetization portion of the field treatment. For the in-plane field treatments, a magnetic field H, applied at an angle θ with respect to the sample plane, was increased to H_{max} and then reduced to 0 T, and the energy was minimized at each field step to obtain the relaxed magnetization configuration, obtained using the relax function. Angles ranging from $\theta = -3°$ to $+3°$ were considered, along with $\mu_o H_{max}$ values of 0.5 to 1.3 T.

Results

The formation of magnetic skyrmions was investigated in the sputter-deposited $[Pt/Co/Ir]_3$ multilayers (Fig. 1(a)). The XRR obtained from a sample deposited under the same conditions but without the Pt capping layer is shown in Fig. 1(b). The fit to the XRR data using the Parratt formalism[27] based GenX program[28] gives layer thicknesses and roughnesses values, as listed in Table I with the designed thickness values for comparison. The layer thicknesses are consistent with the design thicknesses, as expected, and the thin film roughnesses are on the order of a few Angstroms. The hysteresis loops in Fig. 1(c) show that the $[Pt/Co/Ir]_3$ multilayer thin film has perpendicular magnetic anisotropy. The saturation magnetization obtained from the magnetometry measurements is $M_s = 1.1 \times 10^6$ A/m, and the anisotropy, obtained from the area between the in-plane and out-of-plane hysteresis loops in Fig. 1(c), is $K_u = 1.4 \times 10^6$ J/m^3.

<table>
<tr><th colspan="2" rowspan="2">Layer</th><th colspan="2">Fit Parameters</th><th rowspan="2">Design thickness (Å)</th></tr>
<tr><th>Thickness (Å)</th><th>Roughness (Å)</th></tr>
<tr><td colspan="2">Air interface</td><td>N.A.</td><td>3.3</td><td>N.A.</td></tr>
<tr><td rowspan="3">3 ×</td><td>Ir</td><td>9.0</td><td>2.3</td><td>10</td></tr>
<tr><td>Co</td><td>9.7</td><td>4.5</td><td>10</td></tr>
<tr><td>Pt</td><td>12.6</td><td>5.1</td><td>15</td></tr>
<tr><td colspan="2">Ta (buffer)</td><td>16.3</td><td>6.8</td><td>20</td></tr>
<tr><td colspan="2">Substrate</td><td>N.A.</td><td>4.2</td><td>N.A.</td></tr>
</table>

Table I. Thickness and roughness values obtained from fits to the XRR data (Fig. 1(b)) for a substrate/Ta/(Pt/Co/Ir)$_3$ multilayer film.

Figure 2(a) shows a p-MOKE image of the sample taken at remanence ($\mu_o H = 0$ T) after AC demagnetization. The image shows dendritic domains that are ~1 µm wide with rough rather than smooth domain edges. Next, an in-plane magnetic field of $\mu_o H = 0.9$ T was applied, as illustrated in Fig. 2(b), and the remanent state was imaged ($\mu_o H = 0$ T, Fig. 2(c)). Fig. 2(c) shows bubble-like domains with a mean diameter of $d_{sk} = 800 \pm 50$ nm and with cores that point into the plane. The p-MOKE is only sensitive to the normal component of the magnetization and the resolution is diffraction limited hence it is not possible to determine whether the bubbles are bubble skyrmions or not. A comparison with the micromagnetic simulations suggests that the observed bubbles are likely bubble skyrmions.

The experimental field treatment was replicated using micromagnetic simulations of the [Pt/Co/Ir]$_3$ multilayer, firstly to determine if simulations of an idealized multilayer subjected to the experimental in-plane field treatment will lead to bubble skyrmions, and secondly to understand the roles of the DMI, the maximum field magnitude during the in-plane field treatment $\mu_o H_{max}$, and θ. As shown in Figs. 2(d-f), the AC demagnetization and in-plane field treatment ($\mu_o H =$ 1.1 T and $\theta = +1°$) do, indeed, lead to first a dendritic domain pattern followed by skyrmion formation. The magnetic state with $D = 1.6$ mJ/m^2 after an out-of-plane AC demagnetization shows a dendritic domain magnetic configuration (Fig. 2(d)) that resembles the corresponding experimental p-MOKE images (Fig. 2(a)). The magnetic state shown in Fig. 2(d) is the state obtained at the end of the 30-ns AC magnetic field sequence and, while the magnetic field has damped to a negligible level, this magnetization state can be further relaxed. Further relaxation mainly results in smoother domain edges, whereas the domains in Fig. 2(d) have ragged edges. Since the ragged edges are closer to what is observed experimentally, the AC demagnetized state at 30 ns was used as the input magnetization state for the next steps of the field treatment. However, the simulations shown in Fig. 2 were repeated using the fully relaxed AC demagnetized state (run for 30 ns followed by relax) as the input magnetization state for the field treatment and the results were qualitatively similar.

In the simulations shown in Fig. 2(e,g), the in-plane field ($\mu_o H = \mu_o H_{max} = 1.1$ T) was applied at an angle of $\theta = +1°$ with respect to the sample plane. As will be discussed further below, a small misalignment of the in-plane field is needed to promote skyrmion formation. In Figs. 2(e,g) the relaxed magnetization shows a pronounced tilt into the plane and along the direction of the applied magnetic field, i.e., the $+x$ direction, however, the sample is still partially magnetized out-of-plane and domains are still present. The normal component of the sample magnetization in Fig. 2(e) is predominantly in the $+z$ direction (white) with elliptical domains that are tilted in the -z direction (dark). The elliptical domains are long and narrow, and the long axes of the domains are preferentially aligned along the direction of the in-plane component of the applied field. The elliptical domains in Fig. 2(e) are considerably narrower than the dendritic domains in Fig. 2(d) and occupy a smaller area of the sample as compared to the dendritic domains in Fig. 2(d). Fig. 2(f) shows the relaxed magnetic state obtained after the magnetic field is removed ($\mu_o H = 0$ T). Néel-type bubble skyrmions with topological charge $\mathrm{Q} = -1$ are present (Fig. 2(h)) and the polarity of the bubble skyrmions is the same as the residual out-of-plane magnetization component of the domains in Fig. 2(e) (dark, $-z$ direction). Again, the state in Fig. 2(f) qualitatively resembles the corresponding experimental image (Fig. 2(c)). The bubble skyrmion domains form to minimize the total magnetic energy of the system, which includes the DMI, exchange, Zeeman, demagnetization, and magnetic anisotropy energies.

Micromagnetic simulations were used to further investigate the effect of $\mu_o H_{max}$ and θ on the final domain state in the [Pt/Co/Ir]$_3$ multilayers. Figure 3 shows the relaxed magnetization states at $H = 0$ after the magnetic field treatment with $D = 1.6$ mJ/m^2 for a variety of field treatments starting from the demagnetized state shown in Fig. 2(d). The net in-plane magnetizations at $\mu_o H_{max}$ are show in Fig. 1(c) (marked with '×' symbols) and these agree well with the corresponding magnetometry results. At $\mu_o H_{max}$ of 0.5 to 0.9 T and $\theta = 0$ the magnetization of the multilayer increases monotonically with increasing $\mu_o H_{max}$, the multilayer is almost saturated but with small residual domains at 1.1 T (see Fig. 2(c)), and it is fully saturated at 1.3 T. The sample saturates at a lower field with increasing θ since this increases the magnitude of the field along the easy axis. For $\theta = 0°$ domains are observed for all $\mu_o H_{max}$ in Fig. 3, even for 1.3 T where the intermediate state is fully saturated in-plane, whereas single domain out-of-plane states are observed for $\theta > 0$ whenever the intermediate state is a saturated in-plane state. Fig. 3 shows that choosing $\mu_o H_{max}$ that is close to but still below the saturation field combined with a small misalignment of the magnetic field leads to improved skyrmion formation. In all cases the domain walls are Néel-type walls, but the domains are closer to the ideal circular shape of a Néel-type bubble skyrmions when $\mu_o H_{max}$ is close to the saturation field with $\theta = 1 - 2°$.

Figure 4 shows micromagnetic simulations for the same $\mu_o H_{max}$ and θ considered in Fig. 3, but for a larger DMI value of $D = 2.1$ mJ/m^2 and starting from an ac-demagnetized state equivalent to the state shown in Fig. 2(c) but obtained with $D = 2.1$ mJ/m^2. Like what was observed for $D =$ 1.6 mJ/m^2, the field treatment does often lead to bubble skyrmions, and higher percentages of domains that are more circular are found when $\mu_o H_{max}$ is close to the saturation field and slightly misaligned ($\theta = 1 - 2°$). Néel-type bubble skyrmions appear more frequently with the higher DMI, and, furthermore, the percentage of the final state images in Fig. 4 that are occupied by domain walls is higher as compared to the corresponding final state images with $D = 1.6$ mJ/m^2. The area that is occupied by domain walls can be estimated by taking the cell-by-cell average in-plane magnetic moment, and this average increases by ~40% for $D = 2.1$ mJ/m^2 as compared to $D = 1.6$ mJ/m^2. This occurs because the DMI energy decreases with increasing total domain wall length, and this energy reduction becomes more important as compared to other competing energy considerations (demagnetization, anisotropy, Heisenberg exchange) for a larger D.

The effects of the direction of the out-of-plane component of the magnetic field and the sign of the DMI on the formed bubble skyrmions are also important. Figure 5 shows simulations conducted for $D = +1.6$ and -1.6 mJ/m^2 with $\mu_o H_{max} = 1.1$ T applied at $\theta = +1°$ and $-1°$ as well as the AC demagnetized states for the two DMI values. The demagnetized states for $D = +1.6$ and -1.6 mJ/m^2 (Figs. 5(a,b)) are qualitatively similar. The in-plane field treatment with $\mu_o H_{max} = 1.1$ T and $\theta = +1°$ leads to bubble skyrmions with core polarities in the $-z$ direction (Fig. 5(c,d)), whereas with $\theta = -1°$ the skyrmion polarities are in the $+z$ direction (Fig. 5(e,f)) regardless of the sign of the DMI. The DMI sign controls the chirality of Néel-type wall at the boundary of the bubble skyrmions, whereas the direction of the out-of-plane component of the magnetic field used during field treatment sets the direction of the background magnetization and leads to skyrmions with cores in the opposite direction to the applied out-of-plane field.

It is worth noting that bubble domains can be stabilized in the absence of DMI but these domains are often topologically trivial (Fig. 6(c)). Furthermore, as shown in Fig. 6, the sample response to the in-plane field treatment is fundamentally different when the DMI is set to $D = 0$ (Fig. 6(a-c)) as compared to what occurs when $D = 1.6$ mJ/m^2 (Fig. 2(d-f,h) and $D = 2.1$ mJ/m^2 (Fig. 6(d-f)). When $D = 0$, the in-plane field treatment with $\mu_o H_{max} = 0.9$ T and $\theta = 2°$ leads to an expansion of the topologically trivial bubble domain due to the small out-of-plane component of the magnetic field (compare Fig. 6(b) to Fig. 6(a)) and the bubbles relax to smaller bubble domains that are also topologically trivial when H_{max} is removed (Fig. 6c). The bubbles in the final state (Fig. 6(c)) are slightly larger and smoother than those observed after the AC demagnetization (Fig. 6(a)), but the domains are otherwise similar before and after the application of H_{max}. In contrast, for $D = 2.1$ mJ/m^2, the same in-plane field treatment ($\mu_o H_{max} = 0.9$ T and $\theta = 2°$) leads to isolated domains that are elongated along the applied field direction and the subsequent formation of bubble skyrmions when H_{max} is removed, as shown in Figs. 6(e) and (f), respectively. This is similar to the behavior observed for $D = 1.6$ mJ/m^2 (Fig. 2(e-f)). With DMI, the final states (Figs. 2(f) and 6(f), bubble skyrmions) bear little resemblance to the dendritic domains found after the AC demagnetized states (Figs. 2(c) and 6(c)). This transformation observed experimentally in response to the field treatment (Figs. 2(a-c)) more closely resembles the simulations with non-zero DMI, which suggests that the bubbles observed experimentally are indeed skyrmions.

Discussion

The experiments show that the field treatment scheme described here produces skyrmions for a $\mu_o H_{max}$ that is close to but still below the in-plane saturation field of the sample, which is consistent with the simulation results. The simulations further suggest that a small misalignment of the sample during the in-plane field treatment of 1-2° is needed to reliably produce bubble skyrmions. The slight tilt of the sample with respect to the sample plane leads to a normal component of the magnetic field of magnitude $\mu_o H_{max} \sin\theta$ that causes the domains to shrink while the field is turned on as compared to the demagnetized state (compare Figs. 2(d) and (e)). The normal component of the magnetic field during the field treatment sets the direction of the background magnetization (parallel to the field) and consequently the skyrmion core polarities (opposite to the field direction, Fig. 5). It is likely that there is a slight misalignment of the in-plane magnetic field of this order in experiments. Furthermore, the skyrmion polarity after a field treatment run as observed by p-MOKE imaging is consistent across the film, i.e., if the skyrmion cores are in the $+z$ direction in one section of the sample, they are also in the $+z$ direction in other regions, which, according to Fig. 5, is expected for a misalignment that breaks the symmetry.

The mechanism of the skyrmion formation can be understood by examining the images in Fig. 2 more closely and considering the competition between the magnetic energy contributions: DMI, exchange, Zeeman, demagnetization, and anisotropy. The DMI energy density plays an especially important role. The AC demagnetized state (Fig. 2(d)) is comprised of a set of black, dendritic domains magnetized in the $-z$ direction within a film that is otherwise oriented in the $+z$ direction. The black domains are longer than they are wide but there is no preferred orientation for the domain long axes and the domain shapes are irregular. As shown in Fig. 2(e,g), when the treating magnetic field is turned on, the magnetization tilts predominantly towards the direction of the applied field due to the Zeeman energy, and this also lowers the exchange energy since there are large regions of parallel alignment. The applied magnetic field is not quite sufficient to saturate the sample, however, and domains with an out-of-plane tilt, black elongated features that are tilted along the $-z$ direction, are still present. The perpendicular tilt of these domains is favored by the magnetic anisotropy, and the domains also lower the demagnetization energy. The black domains occupy a much smaller area of the image in Fig. 2(e) as compared to Fig. 2(d) because there is a $+z$ component of the applied magnetic field and the Zeeman energy consequently favors a $+z$ tilt of the magnetization. Unlike the domains in the AC demagnetized state, the domains in Fig. 2(e) are long and narrow and, furthermore, the long axes of the domains in Fig. 2(e,g) are along the direction of the applied field, in this case the x-direction. The competition between the exchange, Zeeman, demagnetization, and anisotropy energies explains the presence of the domains in Fig. 2(e,g) as well as the smaller size as compared to the domains in Fig. 2(d) but these energies alone do not explain the domain shape, which stems from the DMI energy as will be explained further below.

When the applied magnetic field is removed, the state in Fig. 2(e) evolves into the bubble skyrmions shown in Fig. 2(f). The smallest domains in Fig. 2(e) disappear when the field is removed, whereas the longer domains in Fig. 2(e) become wider and more circular and ultimately evolve into bubble skyrmions. The black domains occupy a smaller area as compared to the white in Fig. 2(e), which corresponds to a net non-zero magnetization along the $+z$ direction, and Fig. 5 (c-f) shows that there is generally a net remanent moment in the direction of the out-of-plane applied field after relaxation. This is consistent with the magnetometry measurements in Fig. 1(c) that suggest that a non-zero remanent magnetization should be present for a sample tilted such that there is an out-of-plane magnetic field component during the field treatment, and it is also consistent with the MOKE imaging experiments (Fig. 2(c)).

The elongated shape of the domains in Fig. 2(e,g) can be understood by examining the DMI energy, which for a thin film with the symmetry broken along $\hat{z}$ is[29*]

$$E_{DMI} = -L \int \int D \left[\left(m_x \frac{\partial m_z}{\partial x} - m_z \frac{\partial m_x}{\partial x} \right) + \left(m_y \frac{\partial m_z}{\partial y} - m_z \frac{\partial m_y}{\partial y} \right) \right] dx\, dy, \qquad (1)$$

where L is the film thickness and m_i are the components of the magnetization normalized by M_s. As shown in Fig. 2(g), in the presence of a large magnetic field applied along primarily along the x-direction the magnetization in the domain wall regions of an elliptical domain is aligned largely along the x-direction. The magnetization in the domain walls on the left and right sides of the elliptical domain in Fig. 2(g) are aligned along the x-direction, while the domain walls on the top and bottom sides of the domain are tilted slightly along y-axis by approximately 6°.

The first and second terms in Eq. (1) are the main contributions to the energy densities for the domain walls on the left and right sides of the domain in Fig. 2(g), whereas the third and fourth terms are the main contributions to the energy densities for the domain walls on top and bottom of the domain. The magnitudes of the energy densities for the domain walls on the left and right sides of the elliptical domain are large, however, the signs of the energy densities are opposite for the domain walls on the left and right and the net contribution to the DMI energy from these domain walls is consequently small. In contrast, the energy density contributions from the third and fourth terms due to the domain walls on the top and bottom sides of the elliptical domain are both negative and lead to a reduction in the DMI energy. This occurs because the magnetization in the domain walls on the top and bottom sides of a domain tilt slightly along y-axis in the direction favored by

---

* The sign has been adjusted to match the sign convention used in MuMax.

the DMI (in the +(-) y direction on the top (bottom) in Fig. 2(g)). Since this canting of the spins within the domain walls leads to an energy reduction, elongation of the domain along the x-direction (the primary direction of the field) and narrowing of the domain in the y-direction occur. This effect is more pronounced for $\theta = 1°$ as compared to $\theta = 0°$, but for $\theta = 2°$ competition with the Zeeman energy due to the larger out-of-plane field restricts the domain elongation. This domain elongation effect is not present in simulations with $D = 0\ \mathrm{mJ/m^2}$ (Fig 6(b)). When the field is turned off, many of the smaller domains in Fig. 2(e) disappear and the longer domains widen in the y-direction and shrink in the x-direction and evolve into circular or quasi-circular bubble skyrmions with Néel-type walls (Fig. 2(f)). Importantly, no pinning centers are included in the simulations. While pinning centers may also play a role in skyrmion nucleation, the simulations show that the field treatment alone is sufficient to promote skyrmion formation.

As mentioned earlier, the formation of magnetic bubbles in response to a magnetic field has been reported previously for other material systems. A bubble domain phase was found in ultrathin Fe/Ni bilayer films with perpendicular anisotropy[23], and bubble skyrmions were observed in W/CoFeB/Ta/MgO wedge samples[22]. In both cases the bubble-shaped domains formed in response to a large in-plane field with an additional out-of-plane component. The experiments on the Fe/Ni bilayer[23] showed that a non-zero angle between the field and sample plane of up to 10° was needed to form the bubbles, but the authors ruled out incomplete saturation as a mechanism for the bubble formation since the bubbles were observed for a wide range of applied in-plane fields. The Fe/Ni bilayers may have DMI but it is likely weak since a layer with a high spin orbit coupling is not included[24]. In contrast, our work and the experimental results shown in Ref. [22] show that the magnitude of the in-plane field should be kept below the saturation field in order to obtain skyrmions, and that incomplete saturation along with DMI provides a useful avenue to obtaining a bubble skyrmion phase.

We note that the domains and skyrmions in the micromagnetic simulations are smaller than in the experiment, which is likely due to the limited area that was considered in the simulations. Periodic boundary conditions are used in these simulations, and while this helps to provide a more realistic accounting of the long-range demagnetization energy and to reduce edge effects, the size of the main simulation unit, just over $2 \times 2\ \mu\mathrm{m}^2$ for the simulations presented here, still places restrictions on the size of the skyrmions or domains that can form. We ran several tests with a larger simulation area ($4 \times 4\ \mu\mathrm{m}^2$ with $2 \times 2\ \mathrm{nm}^2$ cells) seeded with single skyrmions with diameters ranging from hundreds of nanometers to several micrometers and then relaxed in zero magnetic field. These simulations show several important features. Firstly, the seeded skyrmions relax into bubble skyrmions with similar domain wall profiles but the sizes of the relaxed skyrmions are similar to the sizes of the seeded skyrmions. Secondly, the energy change with skyrmion size is very small with only a <0.3% difference in the total energy for relaxed skyrmions ranging in size from 0.26 to 3.23 μm in diameter. Thirdly, the total energy decreases with increasing skyrmion size, so larger skyrmions are more energetically favorable. These simulations show that the demagnetization and anisotropy energies scale linearly with the skyrmion diameter over the considered size range, which is expected since the skyrmions are large enough that the domain wall energy model should apply[30]. The change in the sum of the demagnetization and anisotropy energies with diameter is small, however, because the slopes of the trend lines are of opposite sign but similar magnitude for the material parameters considered here. Furthermore, the Heisenberg and DMI energies nearly cancel and there is no external magnetic field, so the net exchange and Zeeman energies are small and zero, respectively. Despite the differences in the skyrmion sizes, the bubble skyrmions in the simulations are qualitatively similar to those observed experimentally at the equivalent stages of the field treatment sequence (Fig. 2), and to our experimental MOKE images and simulations.

Conclusions

In summary, p-MOKE imaging shows that a field treatment that consists of an out-of-plane demagnetization step followed by the application and removal of an in-plane field results in the formation of bubble-type skyrmions, and this skyrmion formation process is also observed in simulations. The simulations highlight the importance of choosing an in-plane field that is slightly below the in-plane saturation field, and also show that a small misalignment of the sample is important for promoting skyrmion formation and selecting the skyrmion polarity. Furthermore, increasing the DMI can also lead to more bubble skyrmions. The in-plane field treatment described here provides a simple and reliable way to create magnetic bubble skyrmions, and the simulations provide important guidance on how to improve the skyrmion yield.

Acknowledgements

The authors would like to express their deepest gratitude to Professor Chia-Ling Chien, who has made numerous discoveries in magnetic nanostructures, superconductivity, and spintronics and inspired generations of scientists worldwide. Work at BMC and CSU is supported by the National Science Foundation (DMR #1708790 and #1709525). Work at Argonne National Laboratory (sample growth and experiments) is supported by U.S. Department of Energy, Office of Science, Basic Energy Sciences, Materials Sciences and Engineering Division.

References

[1] K.M. Song, J.S. Jeong, B. Pan, X. Zhang, J. Xia, S. Cha, T.E. Park, K. Kim, S. Finizio, J. Raabe, J. Chang, Y. Zhou, W. Zhao, W. Kang, H. Ju, and S. Woo, Nat. Electron. **3**, 148 (2020).

[2] A. Fert, V. Cros, and J. Sampaio, Nat. Nanotechnol. **8**, 152 (2013).

[3] I. Dzyaloshinsky, J. Phys. Chem. Solids **4**, 241 (1958).

[4] T. Moriya, Phys. Rev. **120**, 91 (1960).

[5] U.K. Rößler, A.N. Bogdanov, and C. Pfleiderer, Nature **442**, 797 (2006).

[6] S. Mühlbauer, B. Binz, F. Jonietz, C. Pfleiderer, A. Rosch, A. Neubauer, R. Georgii, P. Böni, Science (80-.). **323**, 915 (2009).

[7] X.Z. Yu, Y. Onose, N. Kanazawa, J.H. Park, J.H. Han, Y. Matsui, N. Nagaosa, and Y. Tokura, Nature **465**, 901 (2010).

[8] S. Woo, K. Litzius, B. Krüger, M.Y. Im, L. Caretta, K. Richter, M. Mann, A. Krone, R.M. Reeve, M. Weigand, P. Agrawal, I. Lemesh, M.A. Mawass, P. Fischer, M. Kläui, and G.S.D. Beach, Nat. Mater. **15**, 501 (2016).

[9] W. Jiang, P. Upadhyaya, W. Zhang, G. Yu, M.B. Jungfleisch, F.Y. Fradin, J.E. Pearson, Y. Tserkovnyak, K.L. Wang, O. Heinonen, S.G.E. te Velthuis, and A. Hoffmann, Science (80-.). **349**, 283 (2015).

[10] O. Boulle, J. Vogel, H. Yang, S. Pizzini, D. de Souza Chaves, A. Locatelli, T.O. Menteş, A. Sala, L.D. Buda-Prejbeanu, O. Klein, M. Belmeguenai, Y. Roussigné, A. Stashkevich, S. Mourad Chérif, L. Aballe, M. Foerster, M. Chshiev, S. Auffret, I.M. Miron, and G. Gaudin, Nat. Nanotechnol. **11**, 449 (2016).

[11] D.A. Gilbert, B.B. Maranville, A.L. Balk, B.J. Kirby, P. Fischer, D.T. Pierce, J. Unguris, J.A. Borchers, and K. Liu, Nat. Commun. **6**, 8462 (2015).

[12] W. Jiang, S. Zhang, X. Wang, C. Phatak, Q. Wang, W. Zhang, M.B. Jungfleisch, J.E. Pearson, Y. Liu, J. Zang, X. Cheng, A. Petford-Long, A. Hoffmann, and S.G.E. te Velthuis, Phys. Rev. B **99**, 104402 (2019).

[13] C. Moreau-Luchaire, C. Moutafis, N. Reyren, J. Sampaio, C.A.F. Vaz, N. Van Horne, K. Bouzehouane, K. Garcia, C. Deranlot, P. Warnicke, P. Wohlhüter, J.M. George, M. Weigand, J. Raabe, V. Cros, and A. Fert, Nat. Nanotechnol. **11**, 444 (2016).

[14] W. Legrand, D. Maccariello, N. Reyren, K. Garcia, C. Moutafis, C. Moreau-Luchaire, S. Collin, K. Bouzehouane, V. Cros, and A. Fert, Nano Lett. **17**, 2703 (2017).

[15] L. Wang, C. Liu, N. Mehmood, G. Han, Y. Wang, X. Xu, C. Feng, Z. Hou, Y. Peng, X. Gao, and G. Yu, ACS Appl. Mater. Interfaces **11**, 12098 (2019).

[16] W. Li, I. Bykova, S. Zhang, G. Yu, R. Tomasello, M. Carpentieri, Y. Liu, Y. Guang, J. Gräfe, M. Weigand, D.M. Burn, G. van der Laan, T. Hesjedal, Z. Yan, J. Feng, C. Wan, J. Wei, X. Wang, X. Zhang, H. Xu, C. Guo, H. Wei, G. Finocchio, X. Han, and G. Schütz, Adv. Mater. **31**, 1807683 (2019).

[17] J. Sampaio, V. Cros, S. Rohart, A. Thiaville, and A. Fert, Nat. Nanotechnol. **8**, 839 (2013).

[18] N. Romming, Christian Hanneken, Matthias Menzel, Jessica E. Bickel and R.W. Kirsten von Bergmann, André Kubetzka, Science (80-.). **341**, 636 (2013).

[19] Z. Wang, X. Zhang, J. Xia, L. Zhao, K. Wu, G. Yu, K.L. Wang, X. Liu, S.G.E. te Velthuis, A. Hoffmann, Y. Zhou, and W. Jiang, Phys. Rev. B **100**, 184426 (2019).

[20] D. Bhattacharya, S.A. Razavi, H. Wu, B. Dai, K.L. Wang, and J. Atulasimha, Nat. Electron. **3**, 539 (2020).

[21] G. Chen, C. Ophus, A. Quintana, H. Kwon, C. Won, H. Ding, Y. Wu, A.K. Schmid, and K. Liu, Nat. Commun. **13**, 1350 (2022).

[22] K.W. Moon, S. Yang, T.S. Ju, C. Kim, B.S. Chun, S. Park, and C. Hwang, NPG Asia Mater. **13**, 20 (2021).
[23] J. Choi, J. Wu, C. Won, Y.Z. Wu, A. Scholl, A. Doran, T. Owens, and Z.Q. Qiu, Phys. Rev. Lett. **98**, 207205 (2007).
[24] T.N.G. Meier, M. Kronseder, and C.H. Back, Phys. Rev. B **96**, 144408 (2017).
[25] A. Vansteenkiste, J. Leliaert, M. Dvornik, M. Helsen, F. Garcia-Sanchez, and B. Van Waeyenberge, AIP Adv. **4**, 107133 (2014).
[26] D. Khadka, S. Karayev, and S.X. Huang, J. Appl. Phys. **123**, 123905 (2018).
[27] L.G. Parratt, Phys. Rev. **95**, 359 (1954).
[28] M. Björck and G. Andersson, J. Appl. Crystallogr. **40**, 1174 (2007).
[29] S. Rohart and A. Thiaville, Phys. Rev. B **88**, 184422 (2013).
[30] F. Büttner, I. Lemesh, and G.S.D. Beach, Sci. Rep. **8**, 4464 (2018).

Figures

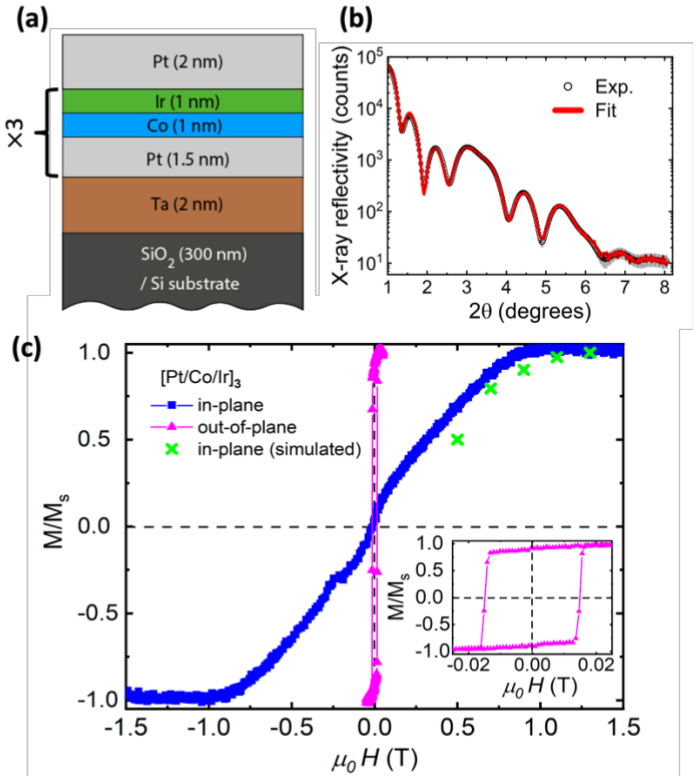

Fig. 1: (a) Schematic of the $[Pt/Co/Ir]_3$ multilayer. **(b)** X-ray small angle reflectivity measurement (symbols) and fit(line) of a $[Pt/Co/Ir]_3$ multilayer. **(c)** Magnetic hysteresis measurements of a $[Pt/Co/Ir]_3$ multilayer with the magnetic field applied out-of-plane (magenta triangles), in-plane (blue squares). The magnetizations obtained from simulations of the $[Pt/Co/Ir]_3$ multilayer for selected magnetic fields applied at an angle of 1° with respect to the sample plane (green x). The inset shows a zoomed-in view of the easy axis (out-of-plane) hysteresis loop.

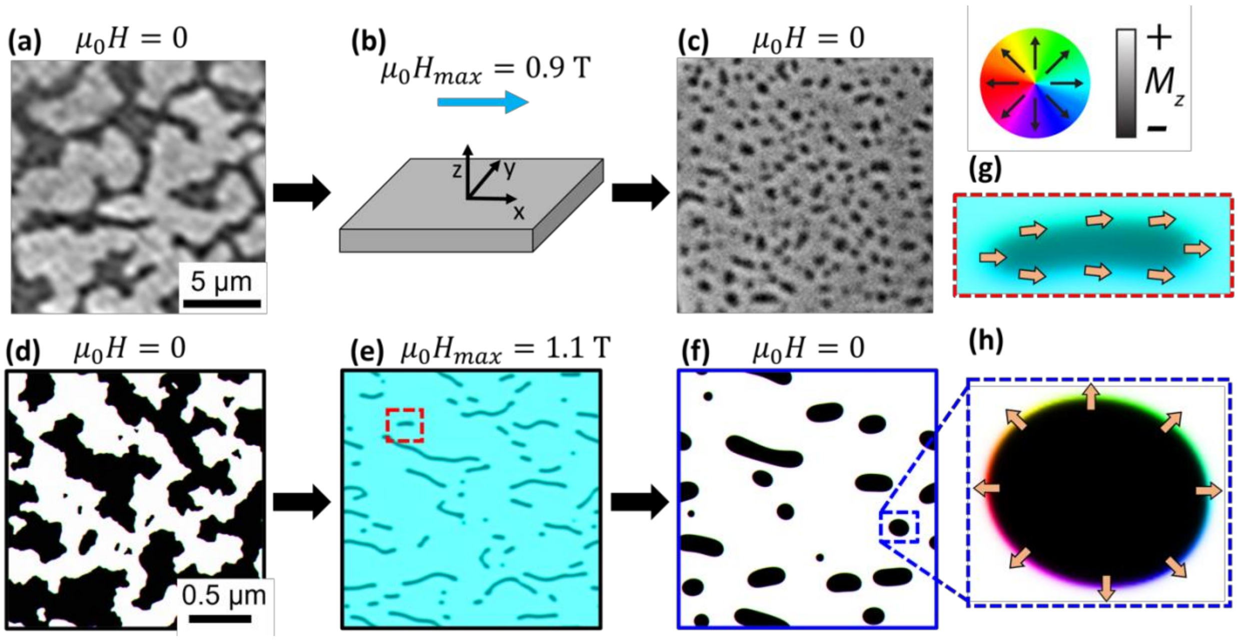

Fig. 2: Experimental polar magneto-optic Kerr effect (p-MOKE) imaging of a $[Pt/Co/Ir]_3$ multilayer **(a)** after AC demagnetization, and **(c)** after applying and removing an in-plane magnetic field with a magnitude of $\mu_o H_{max} = 0.9$ T, as illustrated in **(b)**. Micromagnetic simulations with DMI = 1.6 mJ/m^2 show the magnetic state **(d)** directly after AC demagnetization (at 30 ns), **(e)** the relaxed state at $\mu_o H_{max} = 1.1$ T applied at an angle of one degree with respect to the sample plane, and **(f)** the relaxed state obtained after removing the field. The bubble skyrmions in **(f)** have right-handed chiral Néel walls with topological charge Q = -1. Expanded images of selected domains in **(e)** and **(f)**, outlined by dashed boxes, are shown in **(g)** and **(h)**, respectively. The arrows in **(g)** and **(h)** show the direction of the magnetization at selected positions within the domain walls. The scale bar in **(a)** applies to both **(a)** and **(c)**, and the scale bar in **(d)** applies to **(d-f)**. The coordinate system in **(b)** applies to all experiments and simulations.

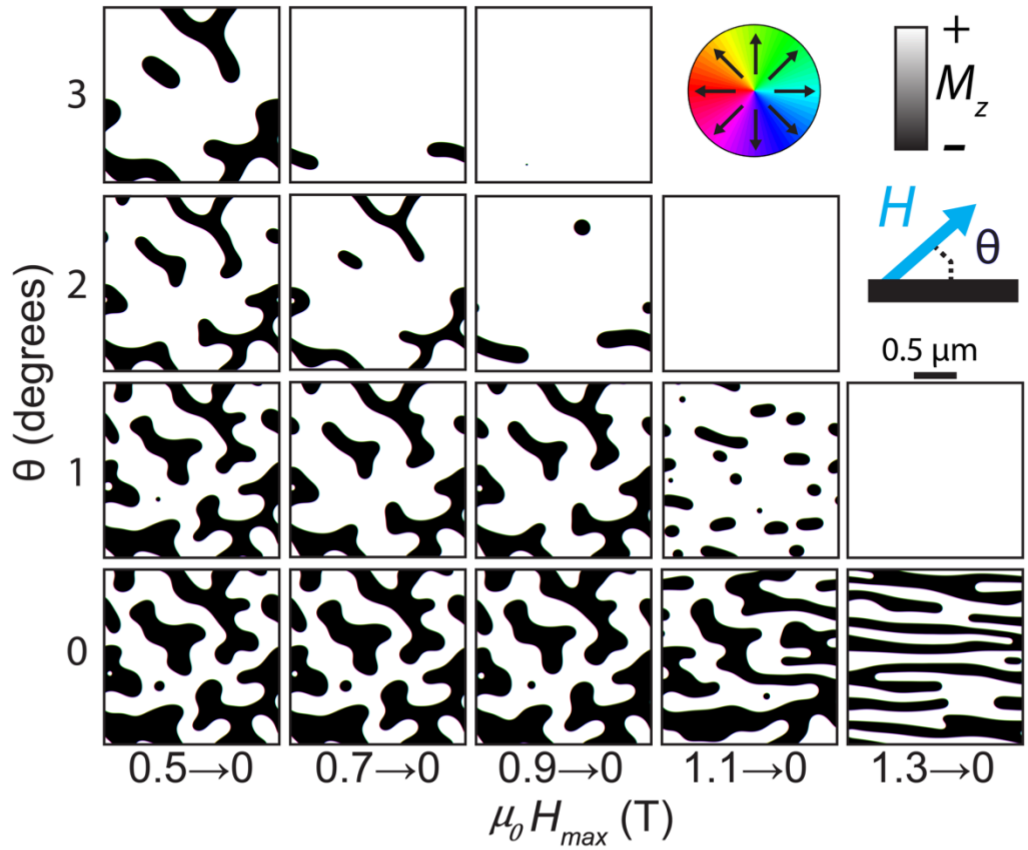

Fig. 3: Micromagnetic simulations with a DMI of 1.6 $\mathrm{mJ/m^2}$ showing the relaxed magnetization states at H = 0 T after magnetic field treatments with $\mu_o H_{max}$ of 0.5, 0.7, 0.9, 1.1, and 1.3 T, for θ, the angle of H with respect to the sample plane, ranging from 0 to 3°. The columns represent the effects of varying H_{max}, and the rows show the effect of varying θ. The domain walls are all right-handed Néel walls.

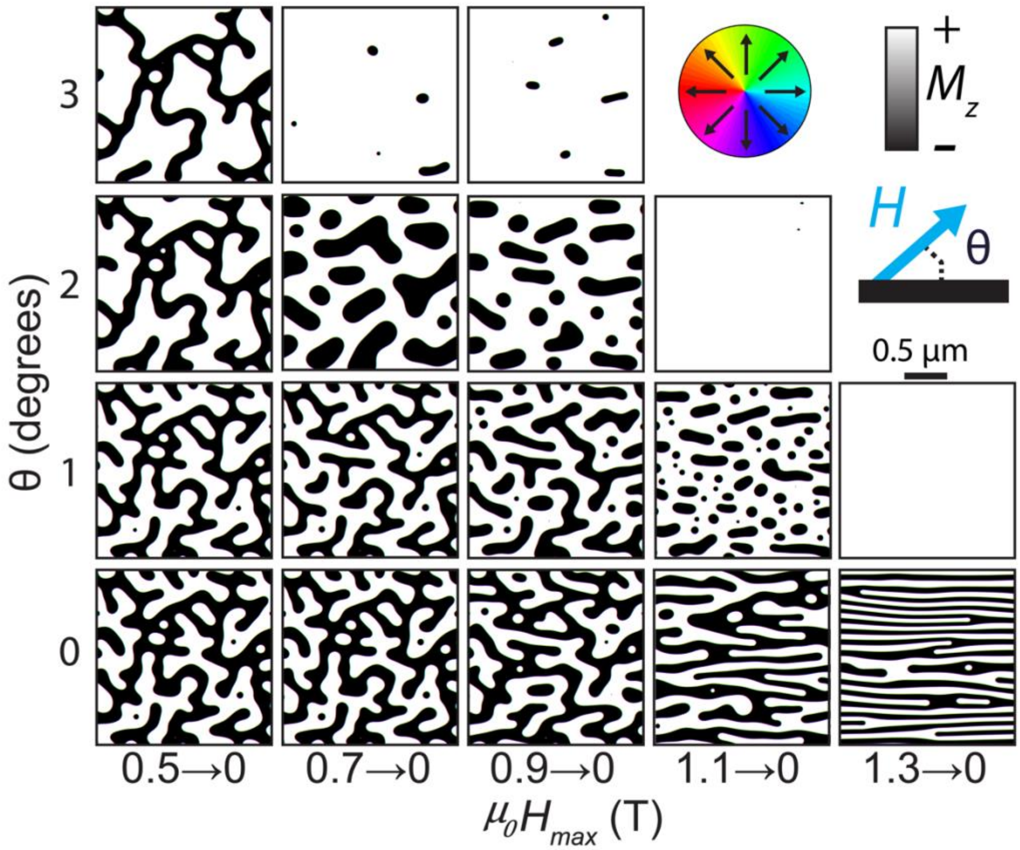

Fig. 4 Micromagnetic simulations with the DMI set to $2.1\ \mathrm{mJ/m^2}$ showing the resulting magnetization states at H=0 after magnetic field treatments with $\mu_o H_{max}$ of 0.5, 0.7, 0.9, 1.1, and 1.3 T for θ from 0 to 3°. The results are organized in the same manner as in Fig. 3. The domain walls are all right-handed Néel walls.

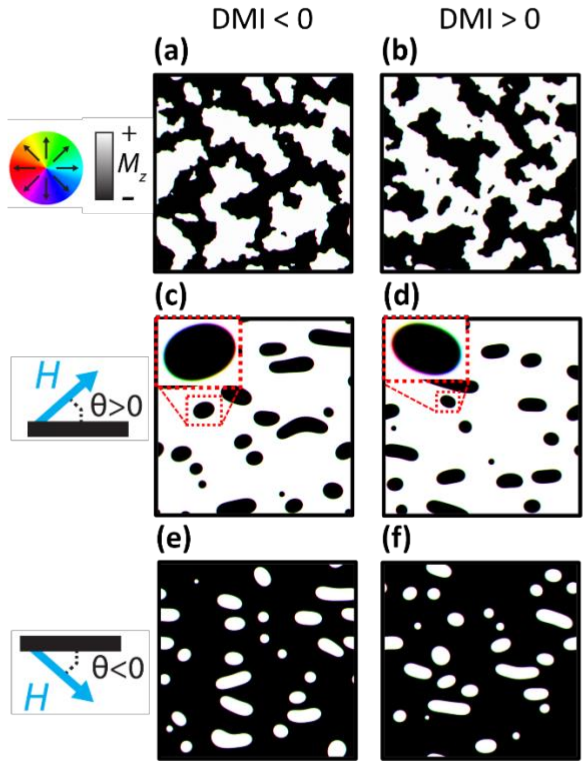

Fig. 5: Micromagnetic simulations of the relaxed magnetic states after AC demagnetization (at 30 ns) with DMI **(a)** - 1.6 $\mathrm{mJ/m^2}$ and **(b)** $+1.6\ \mathrm{mJ/m^2}$ (also the state shown in Fig. 2(d), included here for easier comparison). Magnetization states at $H = 0$ after field treatment with $\mu_o H_{max} =$ 1.1 T applied at **(c,d)** $\theta = +1°$ and **(e,f)** $\theta = -1°$. The DMI was set to + 1.6 $\mathrm{mJ/m^2}$ for **(a,c,e)** and -1.6 $\mathrm{mJ/m^2}$ for **(b,d,f)**. The domains in (c-f) are skyrmions that have right-handed Néel walls with topological charge Q=-1 in **(c,d)**, and left-handed Néel walls with topological charge Q=$+1$ in **(e,f)**.

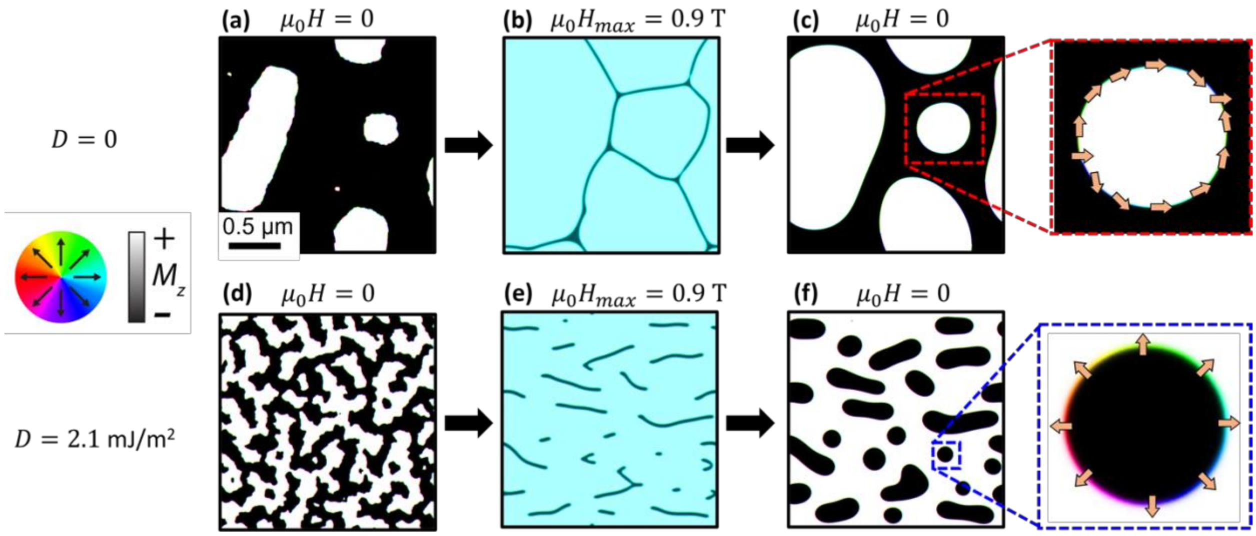

Fig. 6 Micromagnetic simulations with $D = 0$ **(a-c)** and 2.1 mJ/m^2 **(d-f)** show **(a,d)** the magnetic state directly after AC demagnetization (at 30 ns), **(b,e)** the relaxed magnetic state at $\mu_o H_{max} = 0.9$ T applied at $\theta = 2°$, and **(c,f)** the relaxed magnetic state obtained after removing the field. The arrows in **(c)** and **(f)** show the direction of the magnetization at selected positions within the domain walls. The bubble domains in **(c)** have trivial topological charge whereas the bubble domains in **(f)** are skyrmions.